



Cite this: *New J. Chem.*, 2023, **47**, 2847

Combinatorial non-covalent assembly of graphene oxide and chromophores into hybrid nanofilms for organic electronics†

Elizaveta A. Gusarova, Alexandra I. Zvyagina,  Alexey E. Aleksandrov, Alexey A. Averin, Alexey R. Tameev  and Maria A. Kalinina *

A combinatorial method was applied for fabricating functionally different 2D hybrids by using the same starting set of components comprising graphene oxide, perylene chromophore, polydiacetylene surfactant and the salts of divalent ions (Ni(II), Co(II) and Zn(II)) to modulate the properties of resulting systems. The components were assembled through either hydrogen or coordination bonding into layered nanofilms with a thickness 8–20 nm to integrate them into conventional ITO-based cells. Depending on their composition, the hybrids provide different operational characteristics to the resulting devices. The combination of graphene oxide with the light-absorbing polymer exhibits photovoltaic properties, whereas the adding of nickel ions transforms the hybrid into the monopolar conductive layers. The combination of two chromophores gives a multipurpose nanoelement, which performs as either non-linear resistor, diode or photodiode. This strategy can be easily applied to other combinations of chemicals for creating various hybrid nanofilms with targeted functional properties for organic electronics.

Received 28th October 2022,
Accepted 3rd January 2023

DOI: 10.1039/d2nj05281d

rsc.li/njc

Introduction

Ultrathin hybrid materials represent an extensively developing class of nanostructures comprising the advantages of organic compounds with their chemical and functional diversities in combination with mechanical stability, optical and electro-physical properties of inorganic substances.^{1,2} The synergy of interactions between organic and inorganic components due to the charge/energy exchange processes in hybrid structures may lead to the enhancement of properties or even to the emergence of new physical and chemical effects in these materials.^{3,4}

Along with the perovskite-based inorganic films,⁵ hybrid nanofilms capable of converting light into electrical signal are particularly useful for nanoelectronics because they can serve to eliminate some of the most challenging problems in modern photovoltaics, such as high cost, low efficiency, and/or photostability of solar cells.^{6–9} Replacement of traditional silicon solar cells by the hybrid-based ones makes it potentially possible to miniaturize solar cells while increasing their effective

area,^{10,11} and thereby to reduce emissions and waste in their production.

Graphene and its derivatives, graphene oxide (GO) and reduced graphene oxide (rGO), possessing high mechanical strength, flexibility and optical transparency are commonly considered as the best inorganic components among currently applied 2D materials for fabricating ultrathin hybrids with photoelectric properties.^{12–15} The chemical structure of GO presenting various oxygen groups is most suitable for hybridization with organic compounds through covalent and non-covalent functionalization.^{16–19} Thermal or chemical reduction of GO allows partial restoring of conjugation in a carbon carcass to achieve electric conductivity in the GO-based hybrids.^{20–22} The close proximity of the electronic systems of organic molecules and the sp²-conjugated carbon lattice is a key factor for initiating photoinduced charge and/or energy transfer between the components. This transfer can manifest itself as a quenching of fluorescence,^{23,24} high charge mobility²⁵ and the emergence of photoconductivity.²⁶ Depending on the electronic structure of the organic component, the GO layer with its low Fermi level can act as a donor²⁷ or acceptor²⁸ of electrons. This combination of properties makes GO especially promising for fabricating composite GO/organic coatings as photosensitive layers transporting electrons or holes in optically transparent thin-film solar cells.^{29–31}

There are two already developed strategies for integrating GO and organic molecules into ultrathin films, the one-step

Frumkin Institute of Physical Chemistry and Electrochemistry RAS, Moscow, Russia 119071. E-mail: kalinina@phyche.ac.ru

† Electronic supplementary information (ESI) available: NMR spectrum of PDI-PA, SEM microphotos, AFM images, XPS data, absorbance and fluorescence spectra, ellipsometry data, current–voltage curves and energy diagrams of hybrids, AFM images of GO monolayer onto ITO-coated glass. See DOI: <https://doi.org/10.1039/d2nj05281d>

interfacial self-assembly and the liquid-phase epitaxy or, alternatively, layer-by-layer assembly (L-b-L). The adsorption of GO at the air/water interface with spread surfactants³² or other water-insoluble chromophores such as porphyrins³³ followed by the transferring of the as-formed bilayers onto the solids *via* Langmuir–Blodgett or Langmuir–Schaefer techniques allows formation of hybrids with comparatively uniform thickness. However, this method suffers from some limitations such as an elaborated experimental protocol and extreme sensitivity of lateral organization of such films both to deposition parameters and chemistry of supports.

Liquid phase epitaxial deposition of layered films is a labile method adaptable to modern bottom-up technologies associated with production of portable and ultrathin planar devices.^{34–36} By exploiting hydrogen or/and coordination bonding, the epitaxial protocol can be applied for fabrication of the GO-based hybrids with a desirable thickness and composition including ordered assemblies of organic chromophores integrated with GO. We have recently used the epitaxial assembly for producing highly ordered surface-anchored metal–organic frameworks (SURMOFs) from carboxyl- and pyridyl-substituted porphyrin and perylene derivatives on the GO monolayers.^{37,38} The GO sublayer transferred from the oil/water interface onto the solid support provides a planarized template, on which SURMOFs are formed *via* zinc-mediated coordination bonding between the functional groups of GO and organic molecules.

In this work, we adapted this strategy for the ion-mediated epitaxial assembly of structurally different chromophores on the solid-supported GO monolayers. A new combinatorial protocol was developed to create ultrathin hybrid nanofilms with different operational characteristics from a small set of affordable components, a chemical “tool box” containing GO (Fig. 1(a)), 10,12-pentacosadiynoic acid (PCDA) (Fig. 1(b)), perylene derivative *N,N'*-di(propanoic acid)-perylene-3,4,9,10-tetracarboxylic diimide (PDI-PA) (Fig. 1(c)) and divalent salts of Ni(II), Co(II) and Zn(II) (Fig. 1(d)). Graphene oxide was applied as an optically transparent inorganic matrix providing both mechanically stable scaffold for the resulting hybrid and the electron-rich 2D semiconductor. The PCDA surfactant is a UV-polymerizable monomer giving a light-absorbing polymeric semiconductor PDA,³⁹ which may exist in two forms, a highly ordered crystalline blue one and a partially amorphous red one (Fig. 1(b)). Both chromophores were selected because of their high molar extinction coefficients,^{40,41} the presence of carboxyl groups for coordination bonding with divalent metal ions, and their potential ability to participate in the Förster energy transfer between the components due to the overlapping of the emission range of PDI-PA with that of absorption of the red-form PDA.⁴² Although these compounds have already been applied for the light trapping in organic solar cells,^{43–45} they have been deposited either as individual layers or adducts in polymer composites by a conventional spin coating technique yielding comparatively thick surface coatings. In our work, divalent metal ions were used to anchor rather small amounts of these chromophores to the surface through coordination bonding with the carboxyl groups of the components. The salts with different chemistry were used for assessing the effect of the size of metal

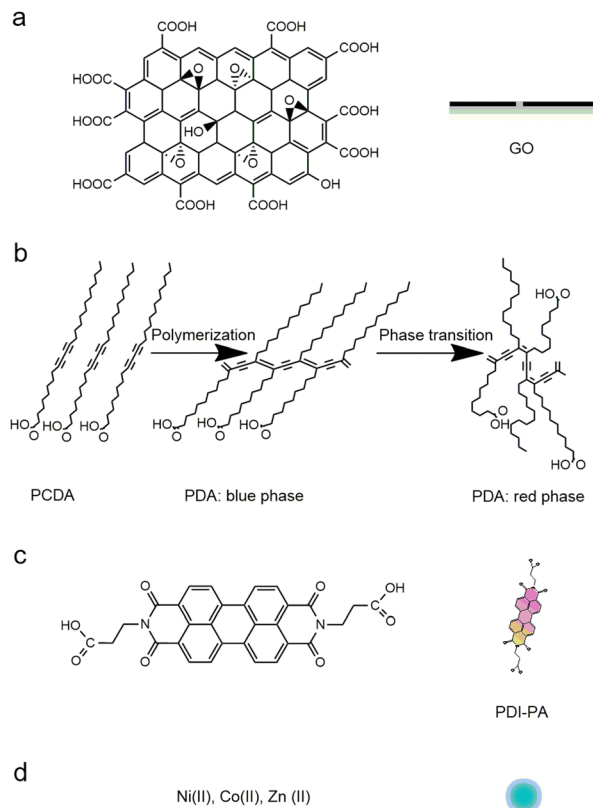


Fig. 1 The structure and schematic representations of the components of a hybrid tool box: (a) graphene oxide (GO), (b) 10,12-pentacosadiynoic acid (PCDA) monomer and polymer forms (PDA), (c) *N,N'*-di(propanoic acid)-perylene-3,4,9,10-tetracarboxylic diimide (PDI-PA), and (d) divalent salts of Ni(II), Co(II) and Zn(II).

ion or cluster on the assembly and properties of the resulting nanofilms to optimize their composition. Different kinds of hybrid nanofilms on solids, GO/PDA, GO/M²⁺/PDA, GO/M²⁺/PDI-PA and GO/M²⁺/PDI-PA/M²⁺/PDA, where M²⁺ is a metal ion, were obtained and studied by UV-vis spectroscopy, fluorescence and Raman spectroscopies, AFM, and XPS methods.

The combinatorial protocol based on coordination bonding between the components makes it possible to expand the functional range of the assembled hybrid nanofilms by varying the order of deposition steps and the combinations of components involved. The functional responses of the as-formed nanohybrids integrated into conventional layered photovoltaic architecture were tuned in a controlled fashion to produce solar cells, electrically conducting layers with monopolar (hole) conductivity, non-linear resistor and photodiode. The strategy used herein may therefore provide a basis for a diversity of new ecology-friendly nanodevices that exhibit stable and predictable functional behavior.

Materials and methods

Materials

GO hydrosol (pH 5.5 ± 0.1) was synthesized from exfoliated graphite powder by a modified Hummers' method described in.⁴⁶ The *n*-hexane, chloroform, ethanol, methanol, Ni(NO₃)₂,

Ni(OAc)₂, Co(NO₃)₂, Zn(OAc)₂, 10,12-pentacosadiynoic acid (PCDA), fullerene (C₆₀) and 4,4',4'-tris[2-naphthyl(phenyl)amino] triphenylamine (2-TNATA) were obtained from Sigma-Aldrich. *N,N'*-di(propanoic acid)-perylene-3,4,9,10-tetracarboxylic diimide (PDI-PA) was obtained from its dianhydride by the synthetic procedure described in⁴⁷ (NMR spectrum is presented in Fig. S1, ESI[†]). Water deionized to 0.2 mS cm⁻¹ conductivity (pH 5.5 ± 0.1) was used for preparation of the GO hydrosol, metal salts and PDI-PA solutions. The PDI-PA solution was prepared as follows: 17 μL of triethylamine was added to 5 ml of PDI-PA aqueous solution with a concentration of 2 × 10⁻³ M, and the solution concentration was increased to 1 × 10⁻⁵ M by dilution with methanol. Polished silicon wafers with native SiO₂ layer and quartz glass supports were purified with a mixture of H₂O₂ and H₂SO₄ in a 1:1 ratio for 20 minutes, then rinsed in deionized water for 20 times and finally dried in a heating oven. ITO-coated glass substrates were pretreated in an ultrasonic bath and oxygen plasma-cleaned. Cleaned supports were kept in the dry atmosphere.

Fabrication of GO monolayers on solid substrates

For fabrication of the GO layers, the 0.4 g L⁻¹ GO dispersions were used. The clean substrates were vertically immersed into the GO dispersion at room temperature and then hexane was poured on the surface of the GO colloid. The interfacial layer of GO was allowed to form for 40 min and then was deposited vertically onto the supports with an automatic dipper. The transferring speed was 1 mm min⁻¹.

Fabrication of GO/M²⁺/PDA and GO/PDA hybrid materials

For the formation of GO/M²⁺/PDA systems by layer-by-layer assembly, the silicon, quartz or ITO-coated glass substrates with deposited GO monolayer were vertically immersed into the 0.005 M solution of the salt of Ni(II), Co(II) or Zn(II) in water in a tempered glass beaker (60 mm in diameter and 40 mm in height) at a room temperature (*T* = 25 ± 1 °C) using an automatic dipper. Then the 589 μL of PCDA solution in a mixed solvent hexane:ethanol 9:1 with concentration of 1 × 10⁻⁴ M was dropped onto the water surface in a chessboard-like manner. The amount of PCDA in the deposited solution was equal to that calculated for a trilayer coating the available surface area with an area per molecule equal to 26 Å². The system was kept for 60 minutes, lifted at a rate of 1 mm min⁻¹ and dried in air.

For fabrication of GO/PDA hybrid materials, a similar procedure was performed without the adding of salt. All PCDA-containing films were irradiated with a VL-6.LC UV lamp (Vilber Lourmat, 12 W, 254 nm) for 2 minutes to polymerize PCDA.

Fabrication of GO/M²⁺/PDI-PA and GO/M²⁺/PDI-PA/M²⁺/PDA hybrid materials

The GO/M²⁺/PDI-PA/M²⁺/PDA hybrid systems were assembled in a stepwise fashion. First, a PDI-PA layer was formed on the GO monolayer surface using an epitaxial assembly by a stepwise immersing the substrate with the GO monolayer into a 0.05 M aqueous solution of the salt of Ni(II), Co(II), Zn(II) and a PDI-PA

solution with a concentration of 1 × 10⁻⁵ M. The substrate was incubated for 30 s in the salt solution, and for 5 min at 20 ± 1 °C in the PDI-PA solution. After each step, the substrate was vertically removed from the corresponding solution at a rate of 1 mm min⁻¹ and dried in air for 20 min.

To obtain GO/M²⁺/PDI-PA/M²⁺/PDA films, the GO/M²⁺/PDI-PA coating was immersed into the solution of the corresponding metal salt. The PCDA layer was formed in a manner similar to that used for the assembly of GO/M²⁺/PDA coatings. To obtain GO/M²⁺/PDI-PA/PDA controls, the GO/M²⁺/PDI-PA coating was immersed into the pure water instead of the salt solution.

For polymerization of PCDA coatings and studying the energy transfer in the as-formed hybrids, the deposited films were irradiated with a VL-6.LC UV lamp (Vilber Lourmat, 12 W, 254 nm) at 1.6 cm distance for different time intervals from 30 s to 2 min.

Fabrication of electronic devices

For constructing electronic devices, the hybrid materials were obtained at ITO-coated glass substrates using the aforementioned protocols applied for their fabrication on the glass and silica supports. For fabrication of the ITO/hybrid material/C₆₀/BCP/Al, the 40 nm C₆₀ and 7 nm BCP layers were deposited by thermal spraying in an M. BRAUN vacuum chamber with a pressure of 10⁻⁴ Pa. For fabrication of the ITO/hybrid material/2-TNATA/Al, the 20 nm 2-TNATA layer was deposited by thermal spraying under the same conditions. Contact layers of aluminum were deposited by thermal spraying through a mask with an area of 0.065 cm².

Ultraviolet-visible (UV-vis) spectroscopy

The absorbance spectra of hybrid materials transferred onto the quartz glass were measured by using a Jasco V-760 spectrophotometer (wavelength accuracy ±0.3 nm, photometric accuracy ±0.002 Abs) in the range 200–800 nm.

Fluorescence

Fluorescence spectra were obtained on a Fluorolog spectrometer (Horiba). The excitation source was a 450 W xenon lamp. The excitation wavelength was 500 nm.

Raman spectroscopy

Raman spectra were obtained with a Renishaw inVia Reflex Microscope system with a 532 nm Nd:YAG laser as excitation source. Laser light was focused on the sample through a 50× objective to a spot size of ~2 μm. The power on the sample was <0.1 mW. The total exposure time ranged from 100 to 1000 s, depending on the sample.

Atomic force microscopy (AFM)

AFM measurements were carried out using Nanoscope V multimode atomic force microscope (Veeco Instruments, Santa Barbara, California). Images were generated in tapping mode in air with high-resolution silicon NSG01 tips (Tipsnano, Tallinn, Estonia) having a spring constant of 5.1 N m⁻¹ and a radius of

curvature of <6 nm. The scan rate was typically 2 Hz. Image processing was performed using the FemtoScan software (Advanced Technologies Center, Russia).

X-ray photoelectron spectroscopy (XPS)

The XPS measurements were performed using a “PREVAC EA15” electron spectrometer. In the current work, Al K α ($h\nu = 1486.6$ eV, 150 W) were used as a primary radiation source. The pressure in analytical chamber did not exceed 5×10^{-9} mbar during spectra acquisition. The binding energy (BE) scale was pre-calibrated using the positions of Ag3d $_{5/2}$ (368.3 eV) and Au4f $_{7/2}$ (84.0 eV) from silver and gold foils, respectively. Samples were supported onto double-sided conducting scotch tape. To take into account the effect of surface charging, the C1s at (Eb = 284.8 eV) from the carbon contamination was used as an internal standard. The spectra were decomposed using Voigt peak fitting function.

Ellipsometry

Spectroscopic ellipsometry measurements were conducted for GO/Ni $^{2+}$ /PDI-PA/Ni $^{2+}$ /PDA hybrid material deposited on a silicon substrate with a 300 nm thick SiO $_2$ layer using an EP4 imaging ellipsometer (Accurion GmbH) using a Nikon 20 \times objective in ambient conditions at room temperature. The samples were illuminated with a laser light at a wavelength of 658 nm. The dielectric permittivity of hybrid film was calculated from experimentally determined real (ϵ_1) and imaginary (ϵ_2) parts of the (complex) dielectric permittivity using the formula:

$$\epsilon = \epsilon_1 + i\epsilon_2$$

Capacity measurements

The capacity was measured with the AKTAKOM AM-3123 system at 1 kHz. The dielectric permittivity values were calculated from the capacitances, taking the average sample thickness as 10 nm.

Measurement of current–voltage characteristics

J - V characteristics of solar cells were recorded by a SMU Keithley 2400 at AM1.5G conditions provided by a solar simulator (Xe lamp 150 W Oriel Solar Simulator, Newport Corp.). The measurements were made with positive and negative potential sweeps in the range from -20 to 20 V. The relative error of J - V measurements was 5%.

Results and discussion

Fabrication and characterization of hybrid nanofilms

For the assembly of all combinations of the components studied herein, the first step was the deposition of the GO nanosheets preliminary adsorbed at the GO hexane/hydrosol interface by a vertical transferring of the GO particles onto the solid support (Fig. 2(a); the method is described in details in⁴⁶). This technique allows formation of uniform GO monolayers over a large area to functionalize the surface with the oxygen-containing groups as well as to smooth out the defects on a surface. This smoothing is important for the appropriate alignment of organic molecules in the layers deposited over the GO sublayer.

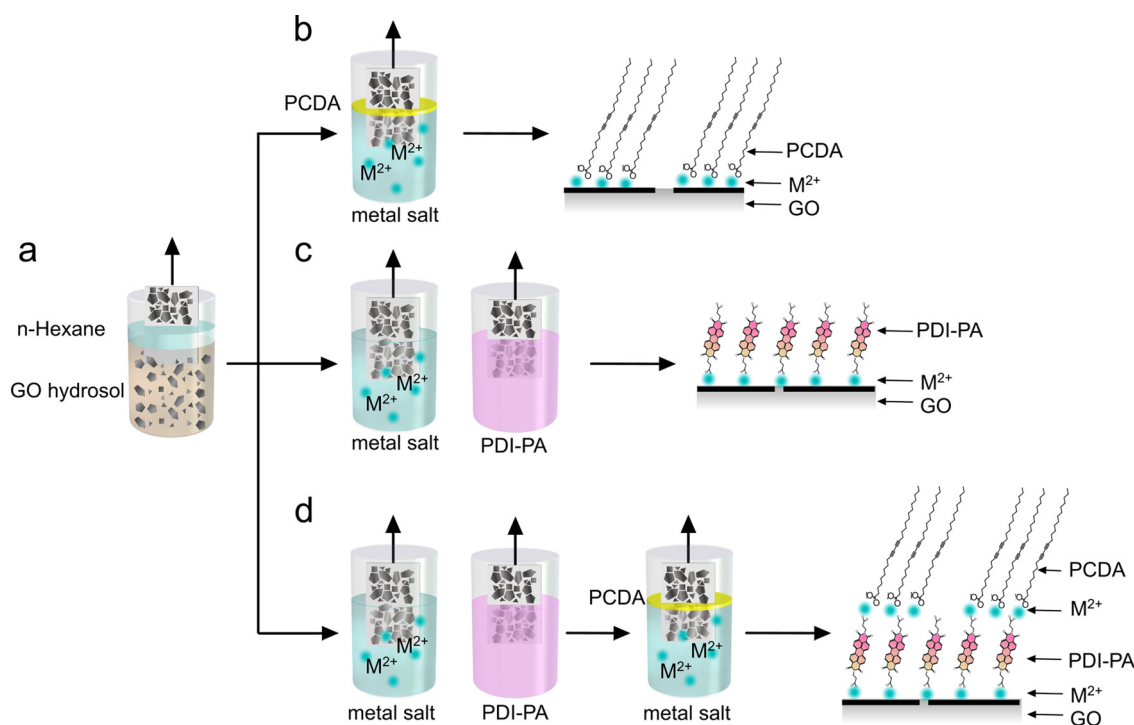


Fig. 2 Schematically illustrated process of a stepwise L-b-L assembly of the ultrathin films with different compositions: (a) GO, (b) GO/M $^{2+}$ /PDA, (c) GO/M $^{2+}$ /PDI-PA, and (d) GO/M $^{2+}$ /PDI-PA/M $^{2+}$ /PDA hybrid materials.

The next step was the deposition of the anchoring layer of the metal ions *via* the binding of M^{2+} by the carboxylic groups presented by the already deposited GO from the aqueous solution of divalent metal salt. This step was performed either prior to the sequential deposition of the chromophore PDI-PA (Fig. 2(c) and (d)) or in combination with the deposition of PCDA after the adsorption of ions on the GO-coated substrate from the subphase with an on-top floating layer of the surfactant (Fig. 2(b) and (d)). The binary and three-component hybrids containing PCDA were irradiated with the UV light after the deposition and drying to transform the monomer into the PDA polymer. The GO/PDA coatings were assembled on the metal-free subphase *via* the same procedure to provide controls.⁴⁸

To obtain binary hybrids from GO and PDI-PA (Fig. 2(c) and (d)), we adapted the stepwise protocol previously developed for the assembling perylene-based SURMOFs on the GO monolayers to avoid the aggregation and further precipitation of the chromophore due to the binding with metal ions.³⁸ The solid substrate with the already deposited GO monolayer was first immersed into the aqueous solution of the salt of Ni(II), Co(II) or Zn(II) and then into the mixed water/methanol solution of PDI-PA.

For integrating the ternary GO/ M^{2+} /PDI-PA/ M^{2+} /PDA hybrid nanofilms, a combination of the aforementioned protocols was applied (Fig. 2(d)). The resulting system is formed *via* hybridization of the inorganic GO scaffold with two organic compounds bonded together by divalent metal ions.

The surfaces of the as-assembled hybrid nanofilms were examined by the scanning electron microscopy (SEM) and the atomic force microscopy (AFM) methods.

The analysis of the SEM images showed that all obtained hybrid films possess similar non-continuous percolative morphologies of the GO sublayer. A patch-like distribution of PDA was found in the samples containing this component (Fig. S2, ESI[†]). For detailed analysis AFM images were used.

Typical morphologies are shown at Fig. 3 using data for hybrids assembled in the presence of $Ni(NO_3)_2$. The GO/ Ni^{2+} /PDA hybrids present the elongated stripes (8–20 nm thick) with a typical shape for crystalline PDA⁴⁸ over the densely packed monolayer of the GO nanosheets (Fig. 3(a)). The GO/ Ni^{2+} /PDI-PA film is a sublayer of GO with the evenly distributed small crystallites with 1.5–2 nm height, which corresponds to a height of the PDI-PA molecule (the structure of PDI-PA molecule was obtained by the semi-empirical PM6 method using a Hyperchem software) (Fig. 3(b)). However, both the amount and uniformity of distribution of PDI-PA crystallites in GO/ Co^{2+} /PDI-PA and GO/ Zn^{2+} /PDI-PA hybrids decreased significantly compared to those in GO/ Ni^{2+} /PDI-PA nanofilm (Fig. S3 and S4, ESI[†]). Most likely, this decrease is a consequence of the differences in stability of the M^{2+} -PDI-PA complexes formed during the assembly (to correctly determine the binding constants for such complexes is an experimentally difficult task due to the presence of amine for preventing PDI-PA dimerization). The morphological picture of the GO/ Ni^{2+} /PDI-PA/ Ni^{2+} /PDA hybrid with a thickness 15–20 nm comprises all these kinds of structural elements (Fig. 3(c)). The integration of components by using nickel salts is therefore preferable for the assembly of such ultrathin hybrid films.

The composition of the hybrid nanofilms was confirmed by a Raman spectroscopy. Two broad bands at 1330 and 1600 cm^{-1} in all obtained spectra correspond to the D and G bands of GO (Fig. 4). In the spectra of the GO/ Ni^{2+} /PDA system, the spectral indications of both red and blue forms of PDA were found in the different examined regions of the same sample (Fig. 4, curves 1 and 2). The characteristic bands of the ordered blue PDA form appeared at 1450 cm^{-1} (C=C oscillation) and 2081 cm^{-1} (C≡C oscillation), and those of the red one – at 1514 cm^{-1} (C=C oscillation) and 2120 cm^{-1} (C≡C oscillation).⁴⁹ Similar spectral picture was obtained for the control metal-free GO/PDA nanofilm assembled through

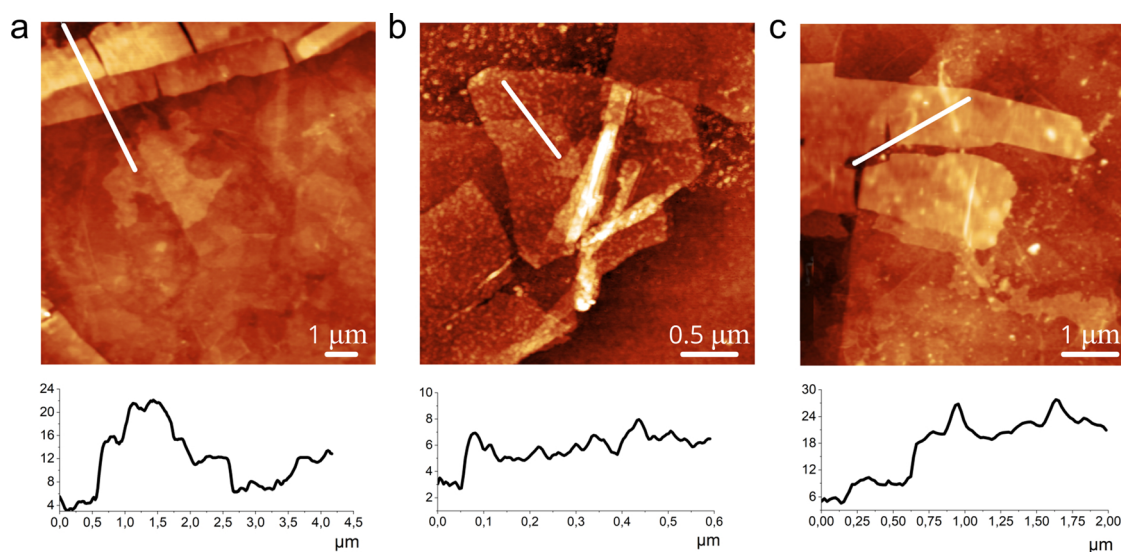


Fig. 3 AFM images and corresponding surface profiles for hybrid nanofilms with different compositions: (a) GO/ Ni^{2+} /PDA, (b) GO/ Ni^{2+} /PDI-PA, and (c) GO/ Ni^{2+} /PDI-PA/ Ni^{2+} /PDA.

H-bonding between GO and PCDA (Fig. 4, curve 3). The presence of the red form of the PDA polymer suggests partial disordering of the polymer chains,⁴⁸ most likely, due to the rearrangement of the head groups of the preorganized PCDA surfactant in a course of its deposition and/or polymerization on the solid-supported GO monolayers.

In the Raman spectrum of the GO/Ni²⁺/PDI-PA nanofilm, the characteristic bands of PDI-PA at 1308, 1355, 1382, and 1587 cm⁻¹^{50,51} are resolved against the background of the wide GO bands (Fig. 4 curve 4). In the control spectrum of the metal-free GO/PDI-PA, no characteristic bands of the chromophore were found suggesting that the PDI-PA molecules did not bind to the GO-coated surface through H-bonding in the absence of the metal ions due to the solvating competition with water molecules (Fig. S5, ESI[†]). Finally, the spectrum of the GO/Ni²⁺/PDI-PA/Ni²⁺/PDA nanofilm shows the bands of all components (Fig. 4 curve 5), and thereby confirms the successful integration of the multicomponent hybrid nanosystem through the epitaxial self-assembly.

To confirm the presence of the nickel ions in the resulting hybrid systems, we applied the X-ray photoelectron spectroscopy (XPS) method. The Si, O, C and Ni peaks were found in the XPS spectra (the full set of XPS spectra is given in Fig. S6, ESI[†]). The presence of nickel within the hybrid films was

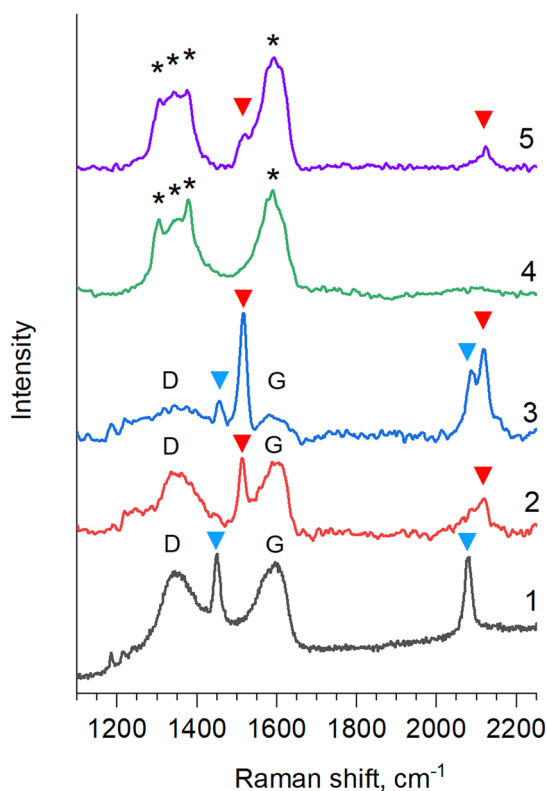


Fig. 4 Raman spectra of hybrid nanofilms with different compositions: (1) and (2) GO/Ni²⁺/PDA film measured at different points of the same sample showing the spectral picture of red (1) and blue (2) forms of PDA, (3) L-b-L GO/PDA, (4) GO/Ni²⁺/PDI-PA, and (5) GO/Ni²⁺/PDI-PA/Ni²⁺/PDA. Asterisks indicate PDI-PA bands, red and blue triangles – bands of red and blue forms of PDA, respectively.

therefore confirmed for the film thickness of at least 10 nm. The shapes of the XPS spectra of the GO/Ni²⁺/PDA, GO/Ni²⁺/PDI-PA and GO/Ni²⁺/PDI-PA/Ni²⁺/PDA in the Ni2p region show close similarity (Fig. 5). All spectra show a strong peak with a maximum at 855.7 eV which is close to the Ni2p_{3/2} signal of Ni(OAc)₂⁵² confirming the binding of nickel ions with the carboxyl groups.

Spectroscopy studies

The ability to absorb visible light by the hybrid nanofilms were investigated by a UV-vis absorption spectroscopy. The characteristic absorption band of GO at 230 nm registered in the control sample of pure GO monolayer (Fig. 6(a) curve 1) was also observed in the spectra of all hybrid materials studied herein. The control spectrum of the metal-free GO/PDI-PA nanofilm merged with that of the pure GO confirming that the chromophore did not adsorb on the surface of GO without metal ions. For the GO/Ni²⁺/PDI-PA system assembled through coordination bonding, two characteristic bands of PDI-PA at 503 and 545 nm were resolved, although the resolution was low due to the small amount of the chromophore material in the ultrathin nanofilm (Fig. 6(a) curve 2). The spectral characteristics of GO/Co²⁺/PDI-PA suggest that only a small amount of perylene molecules is integrated with the resulting film. The presence of Zn²⁺ ions in the GO/Zn²⁺/PDI-PA hybrids promote the aggregation of the PDI-PA molecules (Fig. S7 and S8, ESI[†]). These results complement morphological studies suggesting that the nickel-mediated binding is preferable for fabricating the hybrids with best structural and spectral properties for functioning in planar elements in organic electronic devices.

The GO/Ni²⁺/PDA hybrid system exhibits higher absorption (Fig. 6(a) curve 3) compared to that of the PDI-PA-based binary hybrid. The characteristic absorption bands of both blue and red forms of the PDA polymer were resolved in the UV-vis spectrum.

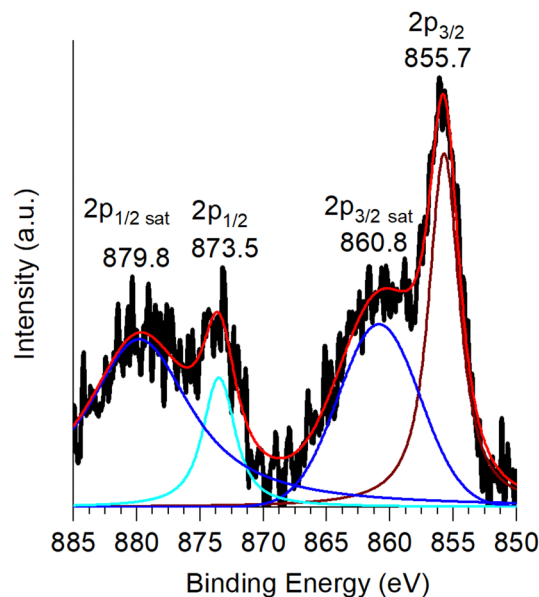


Fig. 5 Typical Ni2p XPS spectrum of the GO-based hybrid nanofilms studied in this work.

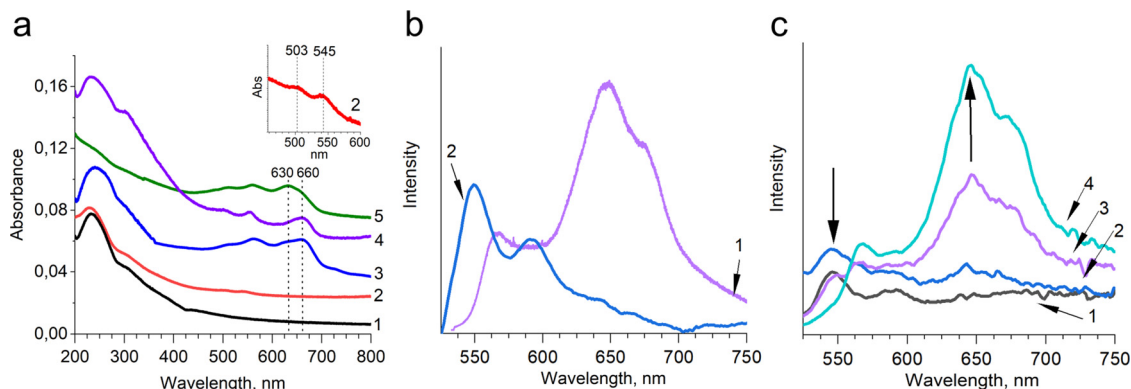


Fig. 6 (a) UV-vis spectra of films of: (1) GO, (2) GO/Ni²⁺/PDI-PA; inset: the characteristic bands of PDI-PA with better resolution, (3) GO/Ni²⁺/PDA, (4) L-b-L GO/PDA and (5) GO/Ni²⁺/PDI-PA/Ni²⁺/PDA; (b) fluorescence spectra of (1) GO/Ni²⁺/PDA and (2) GO/Ni²⁺/PDI-PA hybrid films; (c) fluorescence spectra of GO/Ni²⁺/PDI-PA/Ni²⁺/PDA system recorded after (1) 0 sec; (2) 30 sec; (3) 1 min and (4) 2 min of the UV irradiation onset.

The red form absorbs light at 560 nm, whereas the absorption maximum of the blue one is at 660 nm. The characteristic absorption of the blue form of PDA is known to vary within a wavelength range 640–700 nm depending on the length of polymer chains (the longer the chains, the longer the characteristic absorption wavelength).⁵³ The similar spectral picture was recorded for the ion-free GO/PDA hybrid film assembled through H-bonding between the components (Fig. 6(a) curve 4).

These observations complement those obtained with the Raman spectroscopy and confirm the rearrangement of the PCDA molecules in the deposited films, which packing is somewhat unfavorable for the formation of uniformly planarized polymer fraction.⁵⁴ However, the characteristic band of the blue form in the absorption spectrum of the ternary GO/Ni²⁺/PDI-PA/Ni²⁺/PDA hybrid was shifted toward shorter wavelengths (630 nm) (Fig. 6(a) curve 5). This blue shift suggests that the presence of another chromophore causes the relative shortening of the polymer chains. This effect may be a consequence of the steric hindrance introduced by the PDI-PA itself or due to the distorted (*i.e.*, non-flat) packing of PCDA prior to polymerization on the comparatively rough surface presenting the PDI-PA molecules.

The energy transfer processes between the components in the hybrid nanofilms was studied by a fluorescence spectroscopy. The GO/Ni²⁺/PDA hybrid exhibits the fluorescent properties (Fig. 6(b) curve 1) due to the presence of the red form of the polymer (the blue form of PDA is non-fluorescent).⁵⁵ The characteristic emission peaks appeared at 566 and 645 nm with a distinct shoulder at 670 nm.

Although the absorbance of the chromophore GO/Ni²⁺/PDI-PA hybrid nanofilm was comparatively small, this hybrid shows two strong fluorescence peaks at 540 and 580 nm corresponding to the emission of the PDI-PA derivatives in a monomeric form (Fig. 6(b) curve 2).^{51,56} That is, the energy transfer does not occur between the 2D carbon and the chromophore. This observation suggests that PDI-PA chromophore does interact with the GO surface through coordination to Ni²⁺ rather than through π - π stacking that would lead to a fluorescence quenching due to a close contact between the sp²-system of GO and the aromatic core of PDI-PA.

However, the energy transfer between the chromophores was found in the ternary GO/Ni²⁺/PDI-PA/Ni²⁺/PDA hybrid by studying the kinetics of polymerization of PCDA. The characteristic bands of the PDI-PA monomers were resolved in the spectrum recorded prior to the UV polymerization of PCDA (Fig. 6(c) curve 1). These bands were quenched completely after 2 minutes of UV irradiation of the hybrid film, whereas the characteristic peaks with progressively increasing intensity of emission of the red form of PDA appeared at 566 and 645 nm (the excitation spectra of PDA is given in Fig. S9, ESI[†]). Because the PDI-PA emission overlaps the absorption range of the red form of PDA, the observed spectral pattern is associated with the Förster energy transfer between PDI-PA and PDA molecules (Fig. 6(c) curves 2–4). To confirm the role of metal salt in the energy transfer between organic components in the hybrids, two control systems were assembled. The GO/Ni²⁺/PDI-PA/PDA control was formed to create a direct contact, that is, the shortest possible distance between PDI-PA and PDA molecules. To increase this distance in the GO/Ni²⁺/PDI-PA/Ni²⁺/PDA hybrid, Ni(NO₃)₂ was replaced by Ni(OAc)₂ with a larger anion. The fluorescence studies showed that the fastest energy transfer occurs in a system with direct contact between the PDI-PA and the PDA (Fig. 6(c) and Fig. S10, ESI[†]). The complete quenching of the emission of PDI-PA occurs within 60 seconds. The addition of nickel salts leads to a decrease of the rate of this quenching, which is the slowest in the film formed with Ni(OAc)₂. The energy transfer between the chromophores in these hybrids can therefore be manipulated by altering the size of the incorporating anion of the metal salt. Energy transfer between the perylene core and polydiacetylene backbone has been previously demonstrated for the covalently bonded donor-acceptor counterparts.⁴² Our results represent the first reported example of the energy transfer in the non-covalently assembled supramolecular hybrid comprising these chromophores.

Photovoltaic studies

To assess the potential applicability of our hybrid systems as functional elements in electronic devices, the assembled

nanofilms were integrated with a common ITO/hybrid material/2-TNATA/Al architecture, where 2-TNATA operates as a hole-transport layer (HTL) (Fig. 7). The current–voltage characteristics measured for the control cell ITO/2-TNATA/Al correspond to an ohmic conductivity with high current values (1 A cm^{-2} at 0.5 V) (Fig. S11, ESI†). The deposition of the GO sublayer onto the ITO-coated surface leads to a reasonable decrease of the current by more than an order of magnitude because of the dielectric properties of GO (Fig. S12, ESI†). It should be noted that GO covers the rough surface of ITO as successfully as the surface of glass or silicon (Fig. S13, ESI†).

However, the integration of the ultrathin GO-chromophore hybrids into the cell results in the remarkable changes in the electric response. We have shown earlier that the GO/PDA hybrid integrated with electron-transport layer (ETL) C_{60} showed a photovoltaic behavior due to the PDA/ C_{60} donor–acceptor heterojunction.⁴⁸ In this work, we found that the GO/PDA system exhibits similar behavior in combination with the HTL 2-TNATA layers. The measured ratio of photocurrent to

dark current at -0.15 V on ITO was ~ 3 suggesting that this two-component hybrid nanofilm is a photodiode. The most important aspect of the observed photovoltaic effect is that it occurs even upon absorption of a small number of photons by the ultrathin PDA layer. The short circuit current was as low as $0.16 \mu\text{A cm}^{-2}$, and the open circuit voltage was 0.2 V (Fig. 7(a)). The PDA therefore acts as a photoconductor, whereas the 2-TNATA HTL provides the hole transfer to Al and the GO layer transfers electrons to ITO. These processes are energetically favorable (the energy level diagram is given in Fig. S14, ESI†). Due to the ambipolar conductivity of GO, the GO layer can serve as either ETL in the 2-TNATA-based cell or as HTL in the aforementioned cell with C_{60} .^{27,28}

Thus, the properties of GO make it possible to exploit the GO/PDA nanofilms as a multipurpose functional unit for creating thin-film photodiodes.

When GO and chromophores are integrated with Ni^{2+} ions, the presence of metal induces a nonlinearity of the current–voltage characteristics of the cell. The dark conductivity of the

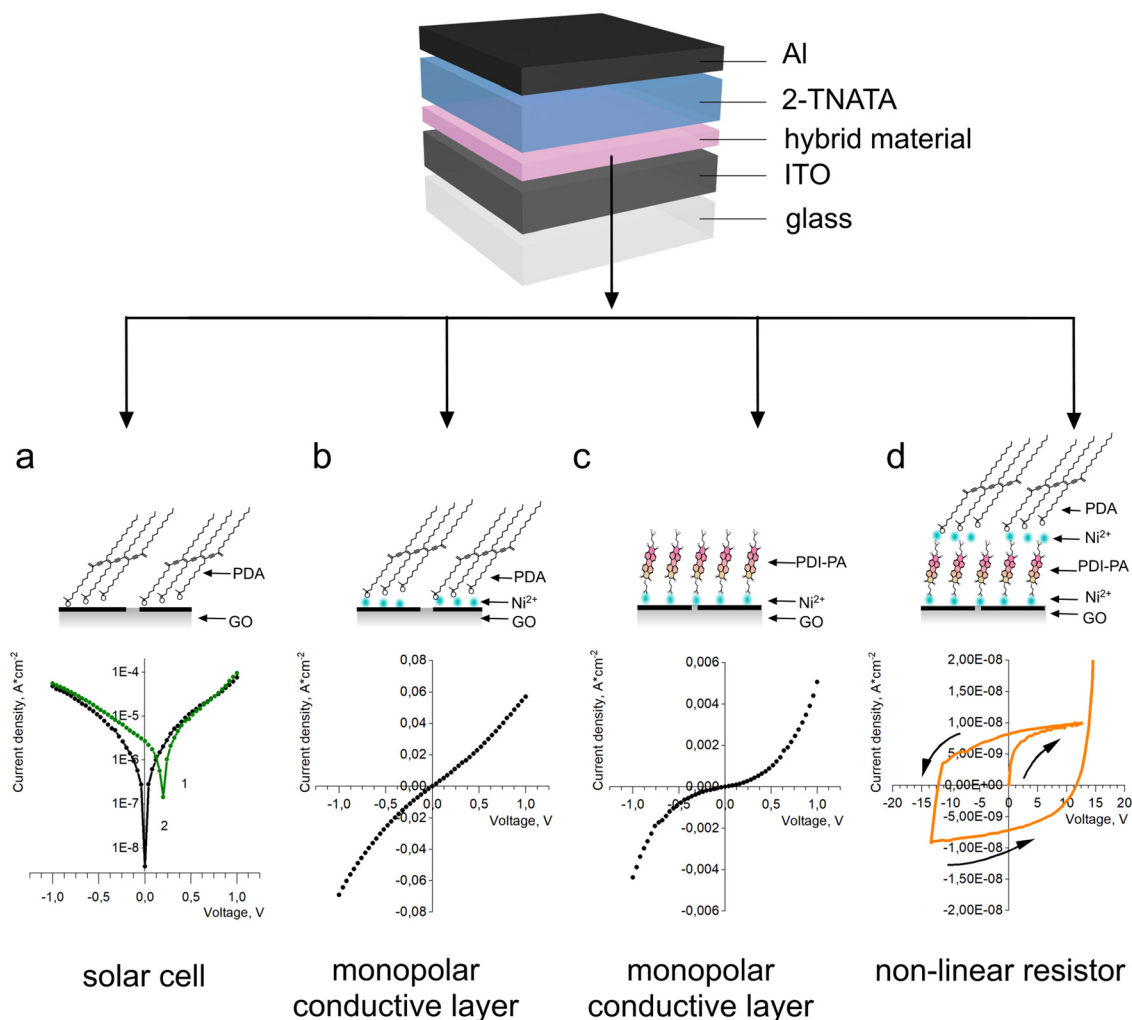


Fig. 7 Schematically illustrated structure and current–voltage dependences of the cells ITO/hybrid material/2-TNATA/Al assembled with different hybrid films: (a) GO/PDA measured for (1) photocurrent and (2) dark current; (b) GO/ Ni^{2+} /PDA for dark current; (c) GO/ Ni^{2+} /PDI-PA for dark current, and (d) GO/ Ni^{2+} /PDI-PA/ Ni^{2+} /PDA for dark current under positive bias on ITO. For the corresponding energy level diagrams, see Fig. S14 and S15 (ESI†).

assembled layered ITO/GO/Ni²⁺/PDA/2-TNATA/Al cell increased significantly up to $6 \times 10^{-2} \text{ A cm}^{-2}$ at 1 V relative to that of the nickel-free system ($8 \times 10^{-5} \text{ A cm}^{-2}$) (Fig. 7(b)). Because of such high dark current, the photocurrent and photovoltaic effect could not be measured in the GO/Ni²⁺/PDA system. This electric behavior is due to the Ni²⁺-associated hole transfer channels between ITO/GO and PDA in both directions, that is, the ITO/GO/Ni²⁺/PDA/2-TNATA/Al cell is a hole-only system. Thus, the GO/Ni²⁺/PDA material with a hole conductivity can be used as an ultrathin conductive layer in electronic devices.

For the cells with integrated GO/Ni²⁺/PDI-PA nano hybrid, we did not observe the photocurrent as well, contrary to our expectations that using a chromophore with a high extinction coefficient ($46\,000 \text{ M}^{-1} \text{ cm}^{-1}$)⁵⁷ would increase the number of photons absorbed by the material (Fig. 7(c)). The dark current in the ITO/GO/Ni²⁺/PDI-PA/2-TNATA/Al structure was $4 \times 10^{-3} \text{ A cm}^{-2}$ at 1 V. This value is more than an order of magnitude lower than that measured in the cell with integrated GO/Ni²⁺/PDA hybrid because the mobility of holes in the PDI-PA based materials ($\sim 10^{-4} \text{ cm}^2 \text{ V}^{-1} \text{ s}^{-1}$)⁵⁸ is lower than that in PDA ($1.3 \times 10^{-3} \text{ cm}^2 \text{ V}^{-1} \text{ s}^{-1}$)⁵⁹. However, the achieved characteristics were insufficient for initiating photovoltaic effects in this cell.

The cell based on the ternary GO/Ni²⁺/PDI-PA/Ni²⁺/PDA hybrid showed nonlinear electric behavior. The measured dark current was at $\sim 10^{-8} \text{ A cm}^{-2}$ at 15 V. The current–voltage curve measured for the dark current both under a positive bias on ITO exhibited a nonlinear character suggesting that this architecture operates as a nonlinear resistor (Fig. 7(d)). A remarkable feature of this device is that it shows nonlinear response at a negative bias on the ITO as well. A hysteresis associated with the bias current appears at the voltage $\sim 15 \text{ V}$. The relatively high values of the threshold voltage of conductivity current are a consequence of the effect of the Coulomb field of Ni²⁺ ions between the PDI-PA and PDA layers. When this ion layer was skipped during the assembly of the cell, the device with this control GO/Ni²⁺/PDI-PA/PDA film showed small threshold voltage and no hysteresis of the current–voltage characteristics (Fig. S16, ESI[†]). The high-frequency optical permittivity of 2.847 system was determined from the ellipsometry measurements of GO/Ni²⁺/PDI-PA/Ni²⁺/PDA using the software of Accurion EP4 imaging ellipsometer (Table S1 and Fig. S17, ESI[†]). This value is in agreement with the low-frequency dielectric permittivity of 3.023 calculated from the capacity measurements at a frequency of 1 kHz. Because of the low dielectric permittivity value, the hysteresis appeared at low currents. The bias current increased by 15–20% upon illumination of the cell owing to the additional charge carriers generated in the chromophores and remained in the traps.

The properties of the GO/Ni²⁺/PDI-PA/Ni²⁺/PDA nano hybrid provides an opportunity to control its electrical conductivity and thereby to apply it as a multipurpose ultrathin module in different conventional architectures of organic solar cells. When this hybrid film was integrated into a cell with C₆₀ as ETL, the functional properties of the resulting device were switched to those of diodes. The as-assembled cell possesses bipolar conductivity, which leads to an increase in the current

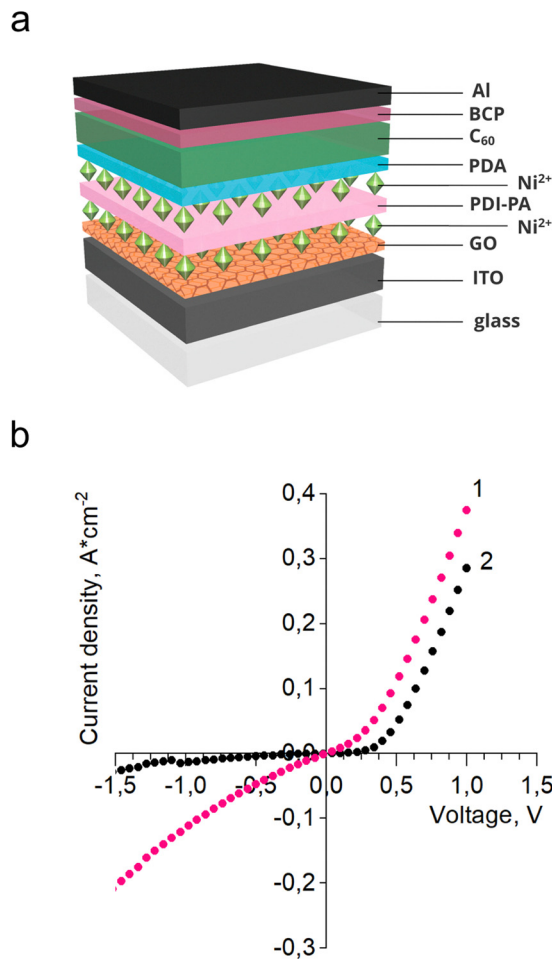


Fig. 8 (a) Schematically illustrated structure of the ITO/GO/Ni²⁺/PDI-PA/Ni²⁺/PDA/C₆₀/Al cell, and (b) corresponding current–voltage dependencies for (1) photocurrent and (2) dark current. For the energy level diagram, see Fig. S18 (ESI[†]).

density at the same voltage values. The ITO/GO/Ni²⁺/PDI-PA/Ni²⁺/PDA/C₆₀/Al architecture (Fig. 8(a)) exhibited the ratio of forward bias dark current (+1 V at ITO) to reverse bias current (−1 V at ITO) ~ 50 suggesting the typical diode behavior. Moreover, this cell also exhibited the photodiode characteristics, as suggested by the photocurrent/dark current ratio of 10 at reverse bias (−1 V at ITO) (Fig. 8(b)). The photoconductivity in the GO/Ni²⁺/PDI-PA/Ni²⁺/PDA hybrid occurs due to the formation of excitons in the PDI-PA chromophore followed by the generation of charge carriers both in the PDI-PA layer during its own excitation and in the PDA layer *via* the transfer of excitation energy from the PDI-PA to the PDA molecules by the Förster mechanism. The Coulomb field of nickel ions can increase the probability of dissociation of these excitons into free electrons and holes, therefore lowering the binding field.

Conclusions

In summary, we demonstrated how to exploit a combinatorial ion-mediated epitaxial assembly for fabrication of ultrathin

hybrid films with different operational characteristic by using a small starting set of components, a hybrid tool box, which includes graphene oxide as a transparent electron–hole transferring layer also providing mechanically stable scaffold for the assembly, a pair of chromophores with overlapping absorption–emission characteristics to initiate energy transfer between them, and divalent metal salts as a source of metal ions to integrate components through coordination bonding as well as to modulate the (photo)electric properties of the resulting hybrids.

By selecting the components and/or by altering the order of the deposition steps, it is possible to assemble binary and ternary ultrathin planar nanohybrids. One of the most remarkable aspects of such systems is the percolative and synergetic character of their functional behavior. Despite their non-continuous morphology with a patch-like distribution of organic domains over the graphene oxide sublayer, they are capable of producing stable and reproducible electric or photoelectric response even at low currents and small amounts of absorbed light. The nanohybrids are compatible with conventional solar cell architectures as well as with other planar organic electronic devices, which functionalities can be tuned by integrating the nanofilms with targeted properties with the appropriately selected electron or hole transporting layers.

Our results therefore provide a set of principles for exploiting hybrid tool boxes in the rational design of functional nanohybrids of this kind. The combination of graphene oxide with the light-absorbing conjugated polydiacetylene polymer provides photovoltaic properties by initiating heterojunction between the polymer and either electron or hole transporting layers. The addition of divalent metal ions transforms such binary hybrids into the elements with a monopolar conductivity due to the formation of metal-induced hole transfer channels. The combination of two chromophores in a single hybrid structure assembled through ion-mediated coordination bonds gives a multipurpose nanoelement, which can be used as either non-linear resistor, diode or photodiode depending on the appropriately selected architecture of the whole cell. When integrated with the hole-transporting layer, the effect of the Coulomb field of the metal ion interlayer will dominate, and the system will show non-linear resistance. When assembled with the electron transporting layer, the Förster energy transfer between the organic components will contribute to the high photoconductivity of the solar cell.

These principles can be applied for creating a wide variety of the GO-based hybrid tool boxes with other potent chromophores and conjugated polymers to achieve the best desirable characteristics for particular kinds of electronic devices or to fabricate multipurpose elements with a number of potential functionalities.

We believe that our strategy is broadly useful for manipulating the properties of the ultrathin functional nanomaterials and for advancing their fabrication toward ecology friendly and resource-saving technologies.

Author contributions

EG and AZ conducted experiments, analyzed data, drafted the manuscript, AEA and AAA contributed analytical tools and

collected data, AT analyzed data, MK proposed a concept of research, contributed to interpretations, revised and approved the manuscript.

Conflicts of interest

The authors declare no competing financial interest.

Acknowledgements

The work is supported by the Russian Science Foundation (grant number 20-13-00279). The Raman, fluorescence and ellipsometry measurements were performed using the equipment of IPCE RAS Joint Research Centre (CKP FMI). XPS analysis was performed by Alexey Sadovnikov using the equipment of the Shared Research Center «Analytical center of deep oil processing and petrochemistry of TIPS RAS. We thank Natalia Samukova (IPCE RAS) for help with ellipsometric measurements. We thank Alexander Ezhov (MSU) for kind assistance with the AFM experiment and Yulia Enakieva (IPCE RAS) for synthesis of PDI-PA.

References

- 1 M. Liras, M. Barawi and V. A. de la Peña O'Shea, *Chem. Soc. Rev.*, 2019, **48**, 5454.
- 2 M. Faustini, L. Nicole, E. Ruiz-Hitzky and C. Sanchez, *Adv. Funct. Mater.*, 2018, **28**, 1704158.
- 3 C. Draxl, D. Nabok and K. Hannelwald, *Acc. Chem. Res.*, 2014, **47**, 3225.
- 4 A. Y. W. Sham and S. M. Notley, *Soft Matter*, 2013, **9**, 6645.
- 5 M. I. H. Ansari, A. Qurashi and M. K. Nazeeruddin, *J. Photochem. Photobiol., C*, 2018, **35**, 1.
- 6 P. Müller-Buschbaum, M. Thelakkat, T. F. Fässler and M. Stutzmann, *Adv. Energy Mater.*, 2017, **7**, 1700248.
- 7 N. Haberkorn, M. C. Lechmann, B. H. Sohn, K. Char, J. S. Gutmann and P. Theato, *Macromol. Rapid Commun.*, 2009, **30**, 1146.
- 8 Z. Zhang, F. Han, J. Fang, C. Zhao, S. Li, Y. Wu, Y. Zhang, S. You, B. Wu and W. Li, *CCS Chem.*, 2022, **4**, 880.
- 9 Z. E. Shi, S. H. Liu, C. H. Tsai, C. W. Li, C. P. Chen and Y. H. Yu, *FlatChem*, 2021, **28**, 100254.
- 10 J. Ramanujam, D. M. Bishop, T. K. Todorov, O. Gunawan, J. Rath, R. Nekovei, E. Artegiani and A. Romeo, *Prog. Mater. Sci.*, 2020, **110**, 100619.
- 11 F. Liu, Q. Zeng, J. Li, X. Hao, A. Ho-Baillie, J. Tang and M. A. Green, *Mater. Today*, 2020, **41**, 120.
- 12 L. Gomez De Arco, Y. Zhang, C. W. Schlenker, K. Ryu, M. E. Thompson and C. Zhou, *ACS Nano*, 2010, **4**, 2865.
- 13 M. Rogala, I. Wlasny, P. Dabrowski, P. J. Kowalczyk, A. Busiakiewicz, W. Kozłowski, L. Lipinska, J. Jagiello, M. Aksienionek, W. Strupinski, A. Krajewska, Z. Sieradzki, I. Krucinska, M. Puchalski, E. Skrzetuska and Z. Klusek, *Appl. Phys. Lett.*, 2015, **106**, 041901.

- 14 J. Wu, H. A. Becerril, Z. Bao, Z. Liu, Y. Chen and P. Peumans, *Appl. Phys. Lett.*, 2008, **92**, 263302.
- 15 H. Park, R. M. Howden, M. C. Barr, V. Bulović, K. Gleason and J. Kong, *ACS Nano*, 2012, **6**, 6370.
- 16 N. Maslekar, P. B. Zetterlund, P. V. Kumar and V. Agarwal, *ACS Appl. Nano Mater.*, 2021, **4**, 3232.
- 17 Y. Liu, B. Sajjadi, W. Chen and R. Chatterjee, *Fuel*, 2019, **247**, 10.
- 18 V. A. Namrata Maslekar, R. A. M. Noor, R. P. Kuchel, Yin Yao and P. B. Zetterlund, *Nanoscale Adv.*, 2010, **2**, 4702.
- 19 S. M. Mousavi, A. Hashemi and M. Arjmand, *ChemistrySelect*, 2018, **3**, 7200.
- 20 V. Agarwal and P. B. Zetterlund, *Chem. Eng. J.*, 2021, **405**, 127018.
- 21 L. G. Guex, B. Sacchi, K. F. Peuvot, R. L. Andersson, A. M. Pourrahimi, V. Ström, S. Farris and R. T. Olsson, *Nanoscale*, 2017, **9**, 9562.
- 22 V. B. Mohan, R. Brown, K. Jayaraman and D. Bhattacharyya, *Mater. Sci. Eng., B*, 2015, **193**, 49.
- 23 Y. Liu, J. Zhou, X. Zhang, Z. Liu, X. Wan, J. Tian, T. Wang and Y. Chen, *Carbon*, 2009, **47**, 3113.
- 24 Q. Luo, R. Ge, S. Z. Kang, L. Qin, G. Li and X. Li, *Appl. Surf. Sci.*, 2018, **427**, 15.
- 25 D. Yu, Y. Yang, M. Durstock, J. B. Baek and L. Dai, *ACS Nano*, 2010, **4**, 5633.
- 26 M. Ilie, D. Dragoman and M. Baibarac, *Phys. Status Solidi*, 2019, **256**, 1800392.
- 27 M. Barrejón, M. Vizuete, M. J. Gómez-Escalonilla, J. L. G. Fierro, I. Berlanga, F. Zamora, G. Abellán, P. Atienzar, J.-F. Nierengarten, H. García and F. Langa, *Chem. Commun.*, 2014, **50**, 9053.
- 28 X. Zhao, X.-Q. Yan, Q. Ma, J. Yao, X.-L. Zhang, Z.-B. Liu and J.-G. Tian, *Chem. Phys. Lett.*, 2013, **577**, 62.
- 29 S. Qu, M. Li, L. Xie, X. Huang, J. Yang, N. Wang and S. Yang, *ACS Nano*, 2013, **7**, 4070.
- 30 G. Kakavelakis, T. Maksudov, D. Konios, I. Paradisanos, G. Kioseoglou, E. Stratakis and E. Kymakis, *Adv. Energy Mater.*, 2017, **7**, 1602120.
- 31 J. C. Yu, J. I. Jang, B. R. Lee, G. W. Lee, J. T. Han and M. H. Song, *ACS Appl. Mater. Interfaces*, 2014, **6**, 2067.
- 32 H. Kim, Y. R. Jang, J. Yoo, Y. S. Seo, K. Y. Kim, J. S. Lee, S. D. Park, C. J. Kim and J. Koo, *Langmuir*, 2014, **30**, 2170.
- 33 E. V. Ermakova, A. A. Ezhov, A. E. Baranchikov, Y. G. Gorbunova, M. A. Kalinina and V. V. Arslanov, *J. Colloid Interface Sci.*, 2018, **530**, 521.
- 34 J. L. Zhuang, A. Terfort and C. Wöll, *Coord. Chem. Rev.*, 2016, **307**, 391.
- 35 A. Y. W. Sham and S. M. Notley, *Langmuir*, 2014, **30**, 2410.
- 36 Y.-B. Tian, Y.-Y. Wang, S.-M. Chen, Z.-G. Gu and J. Zhang, *ACS Appl. Mater. Interfaces*, 2020, **12**, 1078.
- 37 I. N. Meshkov, A. I. Zvyagina, A. A. Shiryaev, M. S. Nickolsky, A. E. Baranchikov, A. A. Ezhov, A. G. Nugmanova, Y. Y. Enakieva, Y. G. Gorbunova, V. V. Arslanov and M. A. Kalinina, *Langmuir*, 2018, **34**, 5184.
- 38 A. K. Reshetnikova, A. I. Zvyagina, Y. Y. Enakieva, V. V. Arslanov and M. A. Kalinina, *Colloid J.*, 2018, **80**, 684.
- 39 K. Takami, J. Mizuno, M. Akai-Kasaya, A. Saito, M. Aono and Y. Kuwahara, *J. Phys. Chem. B*, 2004, **108**, 16353.
- 40 M. Hatada, Y. Sakamoto and A. Katanosaka, *J. Photopolym. Sci. Technol.*, 2002, **15**, 741.
- 41 E. Kozma and M. Catellani, *Dyes Pigm.*, 2013, **98**, 160.
- 42 J. Seo, C. Kantha, J. F. Joung, S. Park, R. Jelinek and J. Kim, *Small*, 2019, **15**, 1901342.
- 43 J. H. Song, T. J. Kang, Y. D. Cho, S. H. Lee and J. S. Kim, *Fibers Polym.*, 2006, **7**, 217.
- 44 P. Muthitamongkol, C. Thanachayanont and M. Sukwattanasinitt, *Curr. Appl. Phys.*, 2011, **11**, S163.
- 45 A. G. Macedo, L. P. Christopholi, A. E. X. Gavim, J. F. de Deus, M. A. M. Teridi, A. R. bin, M. Yusoff and W. J. da Silva, *J. Mater. Sci.: Mater. Electron.*, 2019, **30**, 15803.
- 46 A. I. Zvyagina, E. K. Melnikova, A. A. Averin, A. E. Baranchikov, A. R. Tameev, V. V. Malov, A. A. Ezhov, D. A. Grishanov, J. Gun, E. V. Ermakova, V. V. Arslanov and M. A. Kalinina, *Carbon N. Y.*, 2018, **134**, 62.
- 47 A. Datar, K. Balakrishnan and L. Zang, *Chem. Commun.*, 2013, **49**, 6894.
- 48 E. A. Gusarova, A. I. Zvyagina, A. E. Aleksandrov, N. V. Kuzmina, A. V. Shabatin, A. A. Averin, A. R. Tameev and M. A. Kalinina, *Colloids Interface Sci. Commun.*, 2022, **46**, 100575.
- 49 C. Cui, N. Y. Hong and D. J. Ahn, *Small*, 2018, **14**, 1800512.
- 50 M. Angelella, C. Wang and M. J. Tauber, *J. Phys. Chem. A*, 2013, **117**, 9196.
- 51 J. Wang, W. Shi, D. Liu, Z. J. Zhang, Y. Zhu and D. Wang, *Appl. Catal., B*, 2017, **202**, 289.
- 52 S. O. Grim, W. E. Swartz, L. J. Matienzo and I. Yin, *Inorg. Chem.*, 1973, **12**, 2762.
- 53 G. Wang, Y. Li, X. Huang and D. Chen, *Polym. Chem.*, 2021, **12**, 3257.
- 54 K. Seto, Y. Hosoi and Y. Furukawa, *Chem. Phys. Lett.*, 2007, **444**, 328.
- 55 R. W. Carpick, D. Y. Sasaki and A. R. Burns, *Langmuir*, 2000, **16**, 1270.
- 56 S. Akimoto, A. Ohmori and I. Yamazaki, *J. Phys. Chem. B*, 1997, **101**, 3753.
- 57 C. Ramanan, C. H. Kim, T. J. Marks and M. R. Wasielewski, *J. Am. Chem. Soc.*, 2012, **134**(1), 386.
- 58 C. Huang, S. Barlow and S. R. Marder, *J. Org. Chem.*, 2011, **76**, 2386.
- 59 T. Koyanagi, M. Muratsubaki, Y. Hosoi, T. Shibata, K. Tsutsui, Y. Wada and Y. Furukawa, *Chem. Lett.*, 2006, **35**, 20.